Hindawi Publishing Corporation
Journal of Electrical and Computer Engineering
Volume 2013, Article ID 562548, 9 pages
http://dx.doi.org/10.1155/2013/562548

Research Article

Grid Connection of Wave Power Farm Using an N-Level Cascaded H-Bridge Multilevel Inverter

Rickard Ekström and Mats Leijon

Division of Electricity, Department of Engineering Sciences, Swedish Centre for Renewable Electric Energy Conversion, Uppsala University, P.O. Box 534, 751 21 Uppsala, Sweden

Correspondence should be addressed to Rickard Ekström; rickard.ekstrom@angstrom.uu.se

Received 28 February 2013; Revised 21 May 2013; Accepted 22 May 2013

Academic Editor: Chuanwen Jiang

An N-level cascaded H-bridge multilevel inverter is proposed for grid connection of large wave power farms. The point-absorber wave energy converters are individually rectified and used as isolated DC-sources. The variable power characteristics of the wave energy converters are discussed, and a method of mitigating this issue is demonstrated. The complete power control system is given in detail and has been experimentally verified for a single-phase setup of the 9-level inverter. Theoretical expressions of the power sharing between multilevel cells are derived and show good correspondence with the experimental results.

1. Introduction

In the last decade, a wave energy converter (WEC) concept has been developed and experimentally verified at the Centre for Renewable Electric Energy Conversion, Uppsala University [1–3]. The point-absorber type WEC, shown in Figure 1(a), consists of a linear generator placed on the seabed, connected with a line to the buoy. The generator is of the direct-driven permanent magnet type, with only electrical damping used. The mechanical design is simple and robust to withstand the violent sea states. Since the point-absorber WEC has a natural upper limit in power absorption, the idea is to deploy multiple units, operating as a farm. To reduce the number of sea cables from the offshore farm to the coastline, and also to improve the transmission efficiency, an offshore marine substation is proposed. The substation gathers all the WEC outputs and transfers the power to the electric grid onshore via a single power cable. As a part of the Uppsala University project, a marine substation is under construction, as shown in Figure 1(b). The substation will connect the research wave power farm of multiple WECs to the local grid at 1 kV.

To optimize the absorbed wave power, both mechanical and electrical damping control strategies have been proposed [4–7]. Even though the power absorption may increase, so will the complexity and investment cost of the external circuits. Considering the small-scale nature of the WECs, a simpler strategy may be advantageous. In [8], passive rectification onto a constant DC-bus is evaluated, where the optimal DC-voltage is a function of the sea state.

The selection of transmission technology to shore depends on the power and voltage ratings of the farm and is discussed in [9]. For very remote ocean resources, as for example, offshore wind farms, the capacitive nature of the sea cable urges for the use of a high-voltage direct current (HVDC) link. Only if the plant is within a few km from shore, the medium voltage AC transmission link would be a more cost-efficient alternative.

As the technical evolution of semiconductor devices, like the insulated gate bipolar transistor (IGBT), continuously reach higher voltage and current ratings, the IGBT-based voltage-source inverter (VSI) has become a popular choice for grid connection of renewable energy sources. To reduce the grid current ripple, a passive harmonic filter is put in series with the VSI. This is typically an L or LCL-filter, followed by a stepup transformer. This set-up does not only reduce the system efficiency but also tends to get bulky if put in a marine substation. As an alternative, this paper proposes the cascaded H-bridge multilevel inverter (CHB-MLI) for grid connection of the wave power farm. This topology assumes

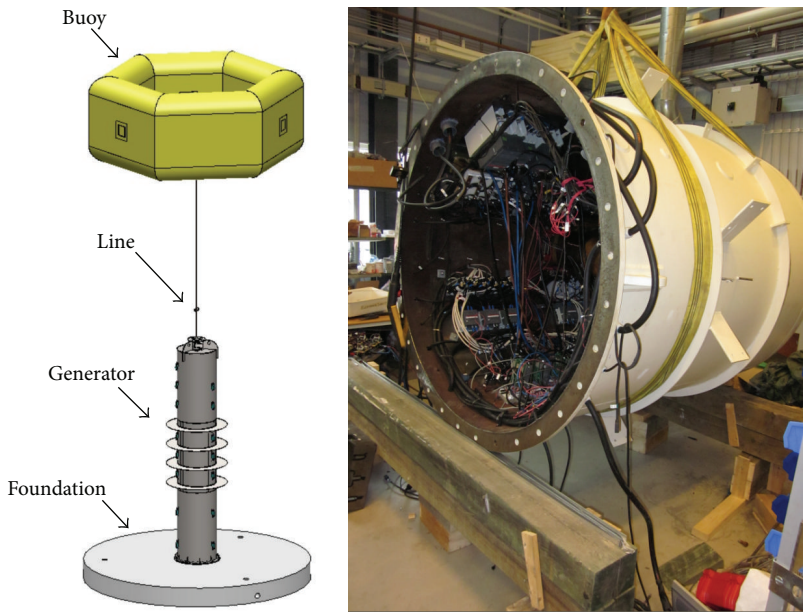

Figure 1: (a) Schematic view of the wave energy converter. The linear generator is put on the seabed and is connected with the buoy through the line. (b) Offshore marine substation for connection of multiple WECs to the onshore electric grid.

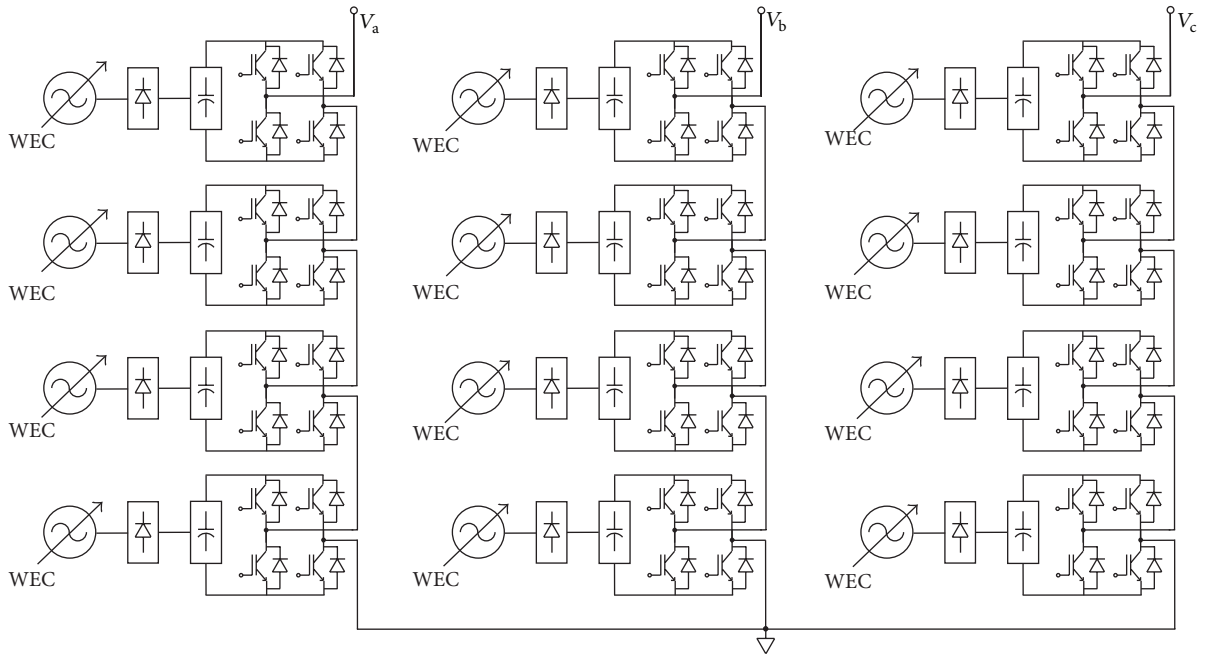

Figure 2: Proposed grid connection topology for a small-scale wave power farm, using the Y-connected 9-level CHB-MLI.

the DC-sources to be electrically isolated, as is the case for the farm. The electrical overview of the proposed scheme is shown in Figure 2 for the three-phase 9-level CHB-MLI in star connection. Few advantages of this topology, compared to the two-level VSI, include

(i) reduced filter size and losses,

(ii) no step-up transformer,

(iii) reduced voltage stresses in the system,

(iv) improved electromagnetic compatibility,

(v) reduced switching losses,

(vi) IGBTs can be rated for lower voltages,

(vii) the individual DC-levels may be optimized for the different WECs;

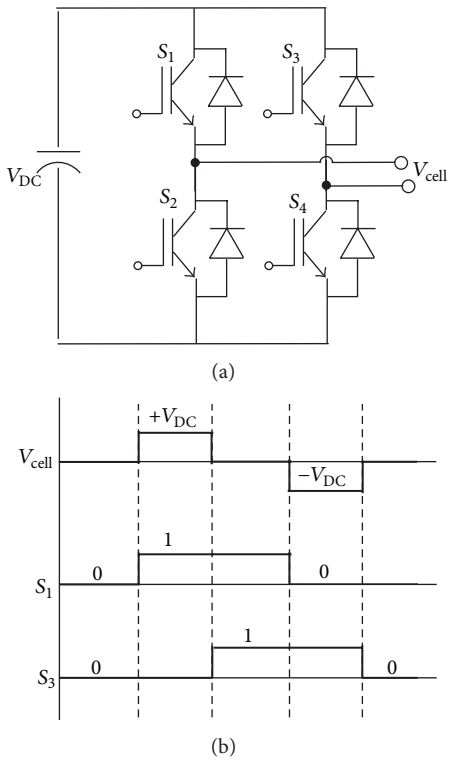

Figure 3: (a) The H-bridge cell unit, consisting of four active devices. (b) The four possible switching states. S_2 is complementary to S_1, and S_4 is complementary to S_3.

while the main drawbacks are

(i) more active devices,

(ii) more complex control system,

(iii) increased conduction losses.

In this paper, the CHB-MLI is proposed for grid connection of a wave power farm. The power flow control from the WECs into the grid is discussed. A simple method of DC-voltage balancing is evaluated. Experimental results on a single-phase 9-level CHB-MLI connected to the grid are presented along with the control system strategy.

2. The Cascaded H-Bridge Multilevel

The CHB-MLI is the most device-efficient of the established multilevel topologies, with respect to the number of output voltage levels. The basic building block cells consist of an H-bridge with four active devices, as is depicted in Figure 3(a). Switches S_1 and S_2 are complementary, as well as the switch pair S_3 and S_4. There are four possible switching states for the H-bridge, resulting in output voltages of $+V_{DC}$, 0 or $-V_{DC}$, as shown in Figure 3(b). By alternating between the two states of zero, all active devices get exposed to the same amount of current.

As long as the DC-sources of all cells are isolated, the cells may be connected in series, as was depicted in Figure 2. This requirement makes the topology suitable for, for example, fuel cells and photovoltaic cells. Its usage has also been suggested for power line conditioning [10], VAR compensation [11], and for motor drives [12]. The output phase voltage is the sum of all cell voltages; that is, $V_{LN} = v_1 + v_2 + v_3 + v_4$. Operating in the linear range, that is, the amplitude modulation $m_a \in [0, 1]$, the total number of levels, m, for the phase voltage is a function of the number of cells, s, according to

$$m = 2\lceil m_a s \rceil + 1, \tag{1}$$

where $\lceil\ \rceil$ is the ceiling function. The number of levels in the line current, l, for the three-phase setup becomes

$$l = 2m - 1. \tag{2}$$

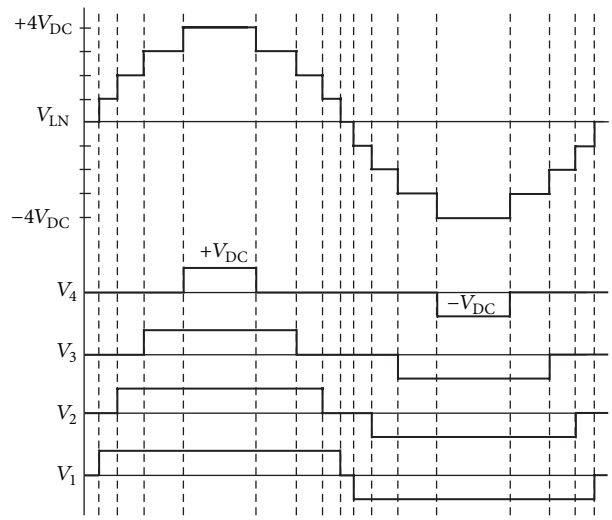

Figure 4: Superposition of the cell voltages for one phase-leg of the 9-level CHB-MLI.

In Figure 4, the superposition principle of the cell voltages is demonstrated. Here, fundamental switching is applied to each cell, meaning that each cell will generate a quasi-square wave.

3. System Voltage Buildup

A major benefit of the CHB-MLI, as stated above, is that all active devices only have to be rated to a fraction of the phase voltage. However, stating that the WECs are isolated from each other is only partially true. In Figure 5(a), the stator windings of a linear generator are shown as mounted in the hull. The hull has direct contact with the sea water, resulting in that the different generators are isolated from each other only by their cable insulation.

In Figure 5(b), two of the generator circuits are displayed. The grounding impedance of each generator, Z_g, is a function of the cable characteristics. All generators in between, when turned on, will add a potential drop of V_{DC} between the generators. The path of a possible voltage buildup in the circuit is illustrated by the red line in Figure 5(b). Assuming that $Z_{g1} = Z_{g2}$, the highest potential drop will occur across

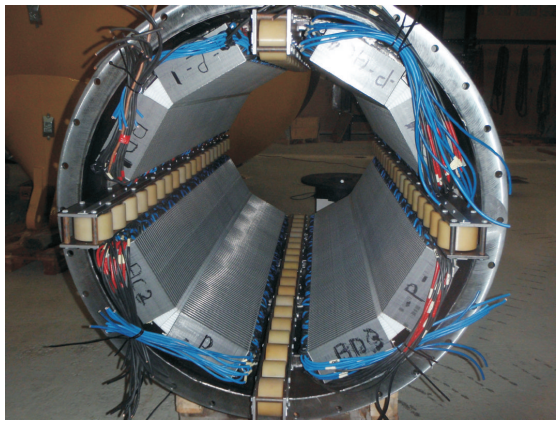

(a)

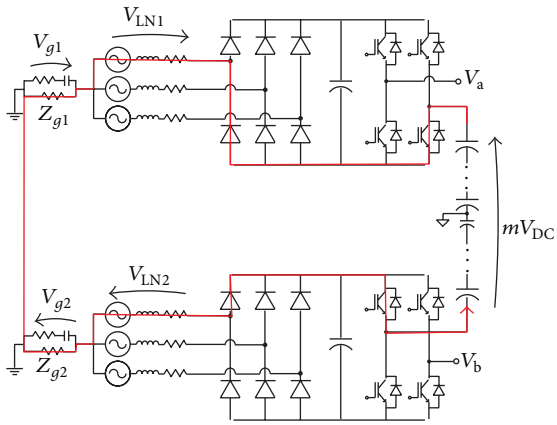

(b)

FIGURE 5: (a) Bottom view of the linear generator, where it can be seen how the stator windings are mounted against the hull. The hulls of the generators in the farm provide a low-impedance path to each other via the sea water. (b) The common ground path through the sea water via their grounding impedances, Z_g, which are dominated by the cable insulation impedance of the stator windings. The red line illustrates one possible path for V_{g1} and V_{g2} to build up. The cable insulation must be rated above this to withstand an electrical breakdown.

the main voltage at $m_a = 1$. The voltage drop across the cable insulation, V_{g1}, can then be expressed as

$$V_{g1} = \frac{\left\lfloor \sqrt{3}\,(s-1) \right\rfloor V_{DC} + V_{LN1} + V_{LN2} - 2V_d}{2}, \tag{3}$$

where $\lfloor\rfloor$ is the floor function and V_d is the diode voltage drop. V_{g1} may be several magnitudes higher than the WEC voltage rating and must be accounted for when selecting cable insulation. This challenge may be solved by putting external insulation covers between the windings and the hull.

4. Switching Control Strategies

There are various suggested modulation strategies of multilevel inverters, where the main three categories are [13, 14]

(i) selective harmonic elimination (SHE),

(ii) space vector modulation (SVM),

(iii) sinusoidal pulse-width modulation (SPWM).

In SHE, the firing angles of each H-bridge are set to either cancel a specific number of harmonics or keep the total harmonic distortion (THD) at minimum [15, 16]. In SVM, the optimal switching state is selected based on feedback control of the current state [17]. It is seldom used for more than three levels due to increased complexity. SPWM is a very popular alternative, not least due to its simple implementation. A carrier wave is compared with a sinusoidal reference wave to turn the switches on or off. Much research has been conducted in optimizing the harmonic output performance by using different types of carrier waves and phase shifting [18, 19]. In Figure 6(a), the phase dissipation (PD) strategy is depicted, in Figure 6(b) the phase opposition dissipation (POD), in Figure 6(c) the alternative phase opposition dissipation (APOD), and in Figure 6(d) the phase shifted (PS) control technique.

5. Power Flow

The purpose of the power control system is to safely transfer the generated WEC powers into the grid at unity power factor. It should also keep the DC-voltage within a range $[V_{DC,low}, V_{DC,up}]$, depending on sea state, to optimize the WEC damping as discussed in Paper [8]. The DC-voltage provides an excellent measure of the system power balance, and by using a DC buffer capacitor, the required system dynamics are reduced. The necessary capacitor size C for each cell of the CHB-MLI depends on the allowed DC-voltage range according to

$$\frac{1}{2}C\left(V_{DC,up}^2 - V_{DC,low}^2\right) = \int_{t_1}^{t_2} \left(P_{WEC}(t) - kP_{grid}(t)\right) dt, \tag{4}$$

where P_{WEC} is the WEC power input and P_{grid} the total power injected in the grid. The variable k gives the relative cell power in proportion to the total power, as will be discussed in Section 5.3.

5.1. WEC Output Power. In deep water, the average power of the waves can be derived using potential wave theory as

$$J = \frac{\rho g^2}{62\pi} T_E H_s^{\,2} \ \text{[W/m]}, \tag{5}$$

where ρ is the water density and g is the gravity constant. The significant wave height H_s and the wave energy period T_E are calculated by

$$H_s = 4\sqrt{m_0}, \qquad T_E = \frac{m_{-1}}{m_0}, \tag{6}$$

where the nth moment of the spectral density $S(f)$ is defined by

$$m_n = \int_0^\infty f^n S(f)\, df. \tag{7}$$

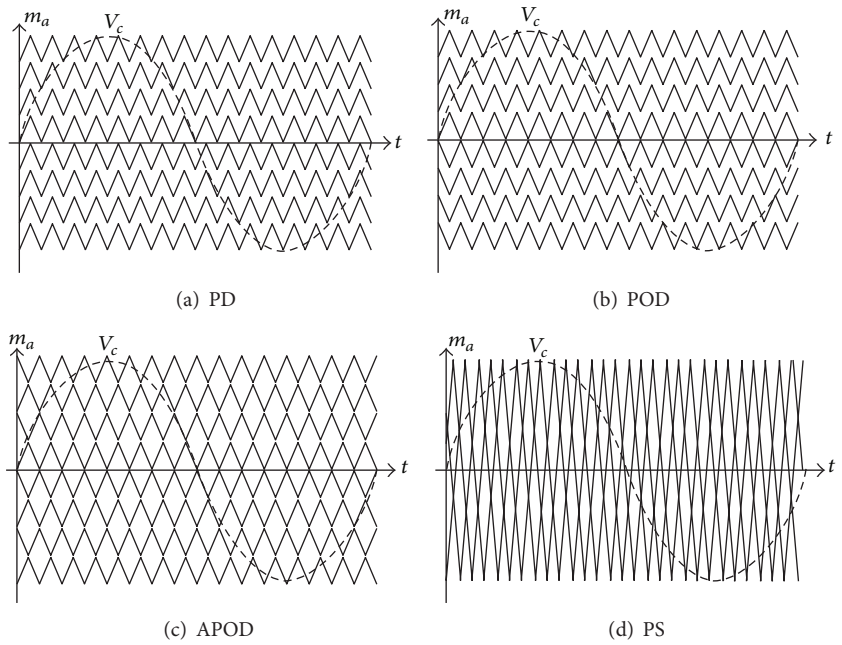

FIGURE 6: Multicarrier SPWM control strategies. The sinusoidal control reference V_c is compared with different types of carrier waveforms to generate the switching logic for the H-bridges.

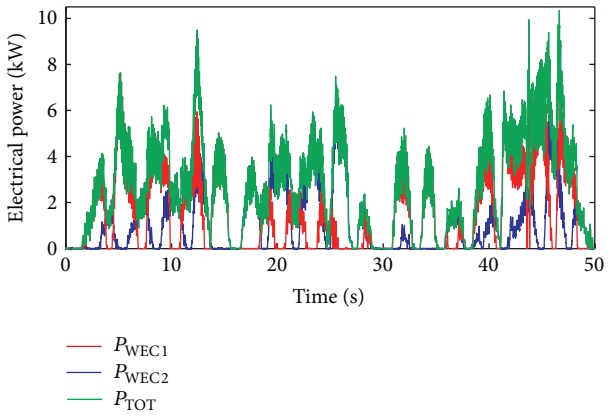

FIGURE 7: The power output from two WECs in real sea trials are displayed [21]. By connecting several units in parallel, the total output power variance can be reduced.

The power absorbed by the WEC varies vastly from 5–40% depending on the sea state [20] as well as the WEC design. The direct-driven WEC, without any intermediate energy storage, will pulsate power twice per wave period. A typical wave energy period of $T_E = 5$ s corresponds to power peaks around 0.4 Hz. In Figure 7 [21], the typical output power of two three-phase WECs under real sea trials is presented. The peak power may be in the order of ten times the average power. By connecting multiple WECs in parallel and distributing their position along the wave direction, the output power variance is much reduced [22].

5.2. Grid Connection Control. Assuming a stiff grid, the single-phase active power P and reactive power Q for a grid-connected CHB-MLI are governed by

$$P = \frac{|V_g||V_i|}{X}\sin(\delta), \qquad Q = \frac{|V_g||V_i|}{X}\cos(\delta) - \frac{|V_g|^2}{X}, \tag{8}$$

where V_g is the grid voltage, V_i the inverter output voltage, δ the load angle, and X the equivalent reactance between the inverter and the grid.

To simplify the current control feedback loop, all phase currents are transformed into the dq0-frame by

$$I_{dq0} = T * I_{abc}, \tag{9}$$

where T is the Clarke/Park transformation matrix [23]

$$T = \sqrt{\frac{2}{3}}\begin{pmatrix} \cos(\theta) & \cos\left(\theta - \frac{2\pi}{3}\right) & \cos\left(\theta + \frac{2\pi}{3}\right) \\ \sin(\theta) & \sin\left(\theta - \frac{2\pi}{3}\right) & \sin\left(\theta + \frac{2\pi}{3}\right) \\ \frac{1}{\sqrt{2}} & \frac{1}{\sqrt{2}} & \frac{1}{\sqrt{2}} \end{pmatrix}. \tag{10}$$

The sinusoidal reference signal V_c, shown in Figure 6, is generated by

$$\begin{aligned} V_c &= V_{cd}^* \cdot \sin(\omega t) + V_{cq}^* \cdot \cos(\omega t) \\ &= m_a \sin(\omega t + \delta), \end{aligned} \tag{11}$$

where V_{cd}^* and V_{cq}^* are current control feedback variables used to control the active and reactive power flows. The amplitude modulation index is $m_a = \sqrt{(V_{cd}^*)^2 + (V_{cq}^*)^2}$, and the load angle is $\delta = \tan^{-1}(V_{cq}^*/V_{cd}^*)$. If $m_a < 1$, the inverter fundamental output rms phase voltage V_{out} is derived as

$$V_{out} = m_a \frac{sV_{DC}}{\sqrt{2}}, \tag{12}$$

where s is the number of cells per phase.

5.3. Power from the Cells. At unity power factor, if the load angle is assumed small and neglecting the internal H-bridge losses, the power drawn from each cell can be calculated as

$$p_{cell}(t) = V_{DC}(t) I_{DC}(t) = V_{cell}(t) I_g(t), \tag{13}$$

where $I_g(t)$ is the grid current and $V_{cell}(t)$ the cell output voltage.

At fundamental switching, assuming the DC-voltage constant and using the quarter symmetry of the waveforms, the average cell power can be expressed as

$$\overline{P}_{cell} = \frac{4V_{DC}}{T} \int_{\theta_n}^{(\pi/2)} I_g(t)\, dt, \tag{14}$$

where T is the fundamental period of the grid voltage and θ_n the angle when the nth cell is triggered. Setting $I_g(t) = \widehat{I} \sin(\omega t)$, this simplifies to

$$\overline{P}_{cell} = \frac{2V_{DC}\widehat{I}_g}{\pi} \cos(\theta_n). \tag{15}$$

If an SPWM-control strategy is used like in Figure 6, the output voltage can be in three different modes, depending on whether the reference signal is above, below, or inside the carrier wave band. In the last case, the cell SPWM-voltage has the same average curvature as the control signal V_c, allowing the following approximation

$$V_{cell} = \begin{cases} 0 & \text{if } 0 \le \theta < \theta_{1n} \\ V_{DC}\left[m_a \sin(\omega t) - \dfrac{s_n - 1}{s}\right] & \text{if } \theta_{1n} \le \theta < \theta_{2n} \\ V_{DC} & \text{if } \theta_{2n} \le \theta \le \dfrac{\pi}{2}, \end{cases} \tag{16}$$

where s_n is the order of the cell. θ_{1n} and θ_{2n} are the lower and upper boundaries of the nth carrier wave band. It is obvious how the relative cell power depends on m_a for SPWM-control. Repeating the derivation of (15) with the cell voltages in (16), the cell power may be derived. In Figure 8, m_a is swept in its linear region, and the relative power distribution between the cells is displayed. Knowing the grid power and m_a, the power from each cell can be calculated. At $m_a = 0.95$, the power distribution between cells is 38.2%, 34.0%, 24.5%, and 3.3%.

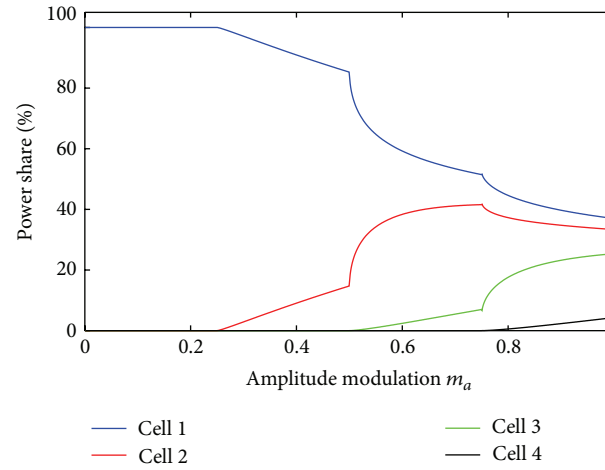

Figure 8: Relative power distribution between the four cells for different m_a, using the PD control strategy.

5.4. Power Control System Layout. The main challenge of the power control loop is to handle the power fluctuations from the WECs. The issue is mitigated, but not resolved, by increasing the size of the buffer capacitors or connecting multiple units to the same capacitor. One solution is to share power between capacitors, where a stronger DC-source is set to temporary charge a weaker DC-source, as discussed in [24].

The benefit of having isolated DC-sources allows for selecting the order of triggering, and may be done at any time during the cycle. In [25], the order of the cells is rotated to get equal discharge of the batteries in an electric vehicles. Similarly, if feedback control is applied on all DC-voltages, the order of rotation may be selected to always start with the highest DC-voltage first. This gives some degree of freedom, limited by the curves of Figure 8. To get further redundancy in the sorting process, more DC-sources may be connected to the CHB-MLI while keeping the number of carrier waves fixed. Such a setup allows for bypassing of cells when their WEC power is low.

In Figure 9, the general power control system block diagram is depicted. The grid connection consists of two feedback loops; an inner current control loop to keep unity power factor and an outer V_{DC}-loop to balance the total DC-level. The system reference frame is obtained by tracking the grid voltage using a phase-locked loop (PLL). All four DC-levels are measured and compared, and the cell with highest DC-voltage is set to trigger first in the SPWM-control. The order is set once per fundamental cycle, but could be updated at any time for improved system dynamics.

6. Experimental Setup

A phase leg of the proposed circuit in Figure 2 has been experimentally implemented. Each H-bridge consists of two dualpackage 400GB126D IGBT modules with inbuilt freewheeling diodes that are shown in Figure 10. The driver boards are mounted in shielded boxes on top of the H-bridges.

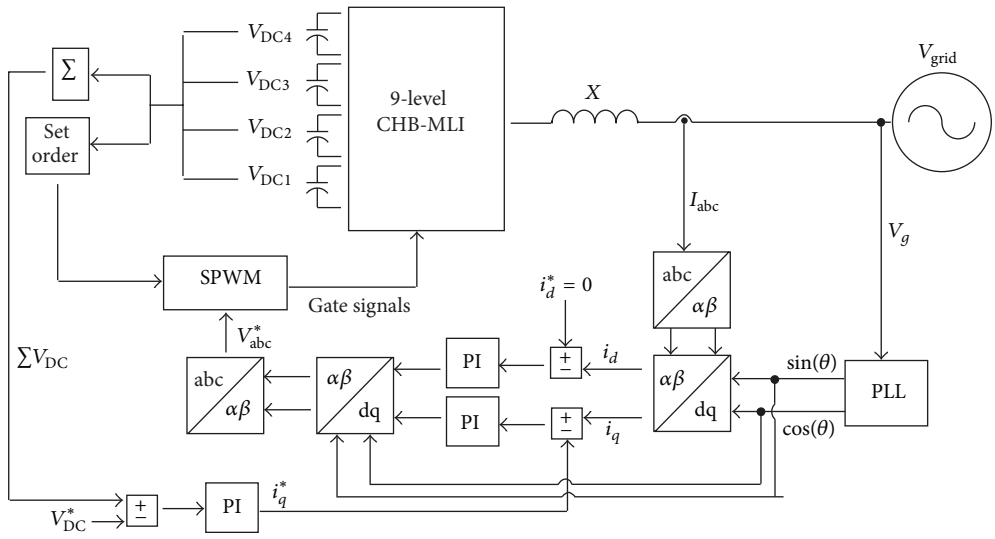

FIGURE 9: Layout of the control system. The total DC-voltage of each phase leg is controlled by varying i_q and thus the load angle to the grid voltage. The individual DC-voltages may be partially controlled by setting the order of conduction of the cascaded H-bridges.

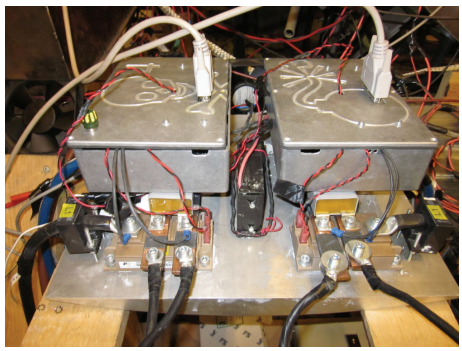

FIGURE 10: Two of the four H-bridge cells, with associated driver circuits mounted in the shielded boxes above the IGBTs.

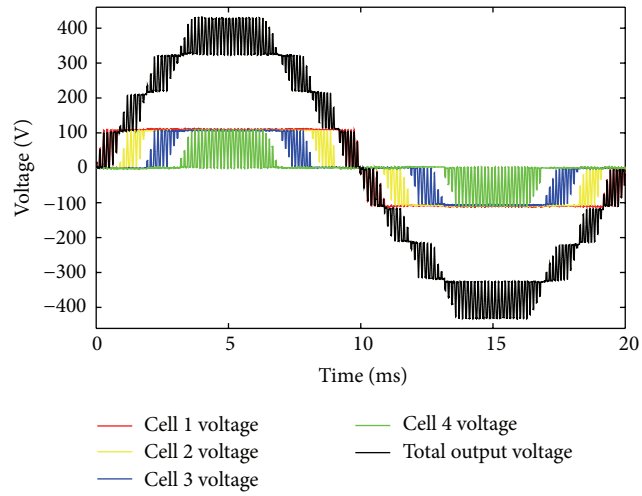

FIGURE 11: Cell voltages and the total output voltage of the 9-level CHB-MLI.

The control system in Figure 9 is implemented in a field-programmable gate array (FPGA) chip, using the PD-SPWM control strategy. The switching frequency of the carrier waveforms was set to 6 kHz, and blanking time between switching states was 2.5 μs.

Four isolated DC-sources at 105 V each were used by rectifying the outputs of a multi-winding transformer. The CHB-MLI was connected to the local grid, at 400 V 50 Hz, through a filter inductor of 3 mH. The grid voltage and DC-voltages were measured with high-frequency differential voltage probes SI-9002, having an accuracy of ±1%. The grid current and DC-currents were measured with current clamps Fluke i310s, having an accuracy of ±2%.

7. Results and Discussion

In Figure 11, the individual cell voltages of the single-phase CHB-MLI have been measured at noload. The amplitude modulation is 0.9, and the output phase voltage has nine levels. In Figure 12, the four cells rotate in order once per fundamental cycle, to vary the power extracted from each DC-source. It is clear that the total output voltage is not affected by the order of the cells, as long as all DC-voltages are similar.

In Figure 13, the 9-level CHB-MLI is connected to the electric grid via a 3 mH inductor, injecting 2 kW at unity power factor. The switching frequency is very attenuated in the current compared to the two-level inverter counterpart. The grid current contains lower order harmonic frequencies due to distortions in the grid voltage.

In Figure 14, the power from each cell has been measured. Assuming a constant DC-voltage, the DC-current are proportional to the power. The relative power from the different cells

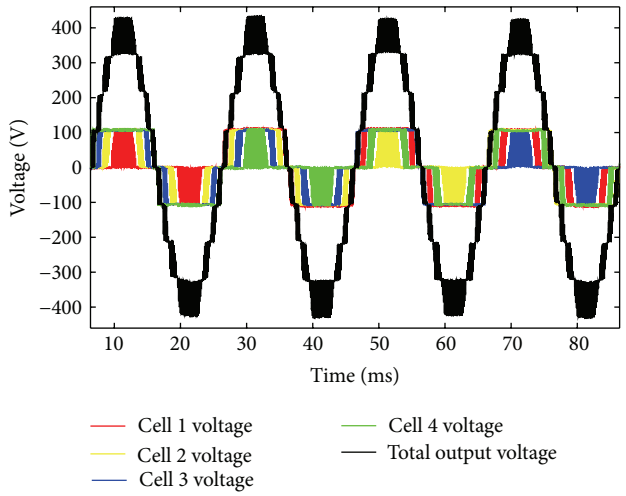

Figure 12: The order of the cell voltages is rotated once per cycle, with the output voltage unaffected.

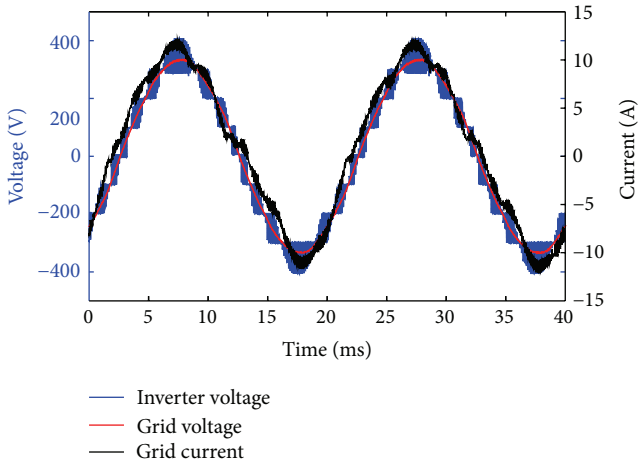

Figure 13: Grid connection of a single-phase 9-level inverter.

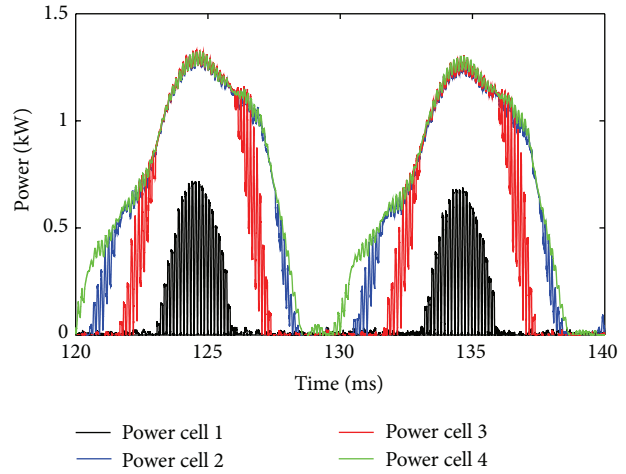

Figure 14: Power output from each cell during one fundamental cycle of grid connection. The power is divided between the cells into 4.3%, 33.6%, 25.5%, and 36.6%, respectively.

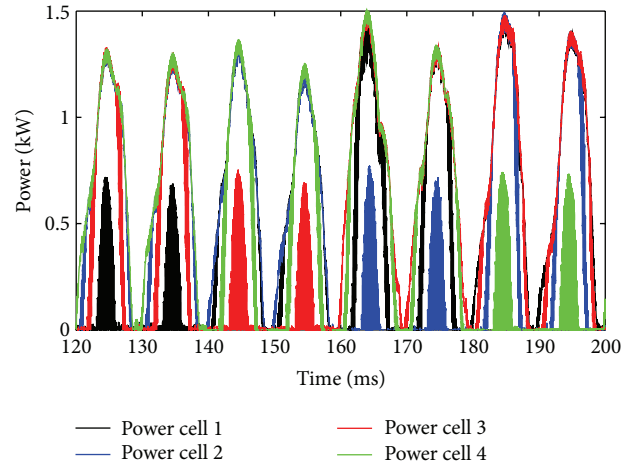

Figure 15: Rotating the cell order to vary the power output from each cell. The average power for four cycles is evenly distributed among the cells.

are 4.3%, 33.6%, 25.5%, and 36.6%, respectively, and m_a for this case was 0.9. This shows very good resemblance with the theoretically derived values in Section 5.3.

In Figure 15, the order of the cells is rotated during grid connection. The average power extracted from each cell during four cycles is very similar for all cells.

8. Conclusion

An N-level cascaded H-bridge multilevel inverter is proposed for grid connection of a large wave power farm. The variable power outputs from the wave energy converters are considered, and the complete power control system for grid connection is demonstrated. By rotating the conduction order of the cells, more power may be extracted from the cells with more energetic WECs connected. A single-phase setup of the 9-level CHB-MLI has been connected to the grid, and the power has successfully been varied according to theory.

Acknowledgments

The Lysekil Project is supported by Statkraft AS, KIC InnoEnergy-CIPOWER, Fortum oy, the Swedish Energy Agency, Draka Cable AB, the Gothenburg Energy Research Foundation, Falkenberg Energy AB, the Wallenius Foundation, Helukabel, ProEnviro, Seabased AB, the Olle Engkvist Foundation, the J. Gust. Richert Foundation, Ångpanneföreningen's Foundation for Research and Development, CF Environmental Fund, the Göran Gustavsson Research Foundation, Vargöns Research Foundation. And This support is gratefully acknowledged.

References

[1] M. Eriksson, R. Waters, O. Svensson, J. Isberg, and M. Leijon, "Wave power absorption: experiments in open sea and simulation," *Journal of Applied Physics*, vol. 102, Article ID 084910, 5 pages, 2007.

[2] O. Danielsson, M. Leijon, K. Thorburn, M. Eriksson, and H. Bernhoff, "A direct drive wave energy converter—simulations and experiments," in *Proceedings of the 24th International Conference on Offshore Mechanics and Arctic Engineering (OMAE '05)*, pp. 797–801, June 2005.

[3] M. Leijon, H. Bernhoff, O. Ågren et al., "Multiphysics simulation of wave energy to electric energy conversion by permanent magnet linear generator," *IEEE Transactions on Energy Conversion*, vol. 20, no. 1, pp. 219–224, 2005.

[4] H. Luan, O. C. Onar, and A. Khaligh, "Dynamic modeling and optimum load control of a PM linear generator for ocean wave energy harvesting application," in *Proceedings of the 24th Annual IEEE Applied Power Electronics Conference and Exposition (APEC '09)*, pp. 739–743, February 2009.

[5] J. K. H. Shek, D. E. Macpherson, and M. A. Mueller, "Experimental verification of linear generator control for direct drive wave energy conversion," *IET Renewable Power Generation*, vol. 4, no. 5, pp. 395–403, 2010.

[6] P. Ricci, J. Lopez, M. Santos et al., "Control strategies for a wave energy converter connected to a hydraulic power take-off," *IET Renewable Power Generation*, vol. 5, no. 3, pp. 234–244, 2011.

[7] D. Valério, P. Beirão, and J. Sá da Costa, "Optimisation of wave energy extraction with the archimedes wave swing," *Ocean Engineering*, vol. 34, no. 17-18, pp. 2330–2344, 2007.

[8] R. Ekström, V. Kurupath, C. Boström, O. Svensson, R. Waters, and M. Leijon, "Evaluating constant DC-link operation of a wave-energy converter," in *Proceedings of the ASME 31st International Conference on Ocean, Offshore and Arctic Engineering*, 2012.

[9] K. Thorburn, H. Bernhoff, and M. Leijon, "Wave energy transmission system concepts for linear generator arrays," *Ocean Engineering*, vol. 31, no. 11-12, pp. 1339–1349, 2004.

[10] F. Z. Peng, J. W. McKeever, and D. J. Adams, "Power line conditioner using cascade multilevel inverters for distribution systems," in *Proceedings of the IEEE 32nd IAS Annual Meeting on Industry Applications Conference*, pp. 1316–1321, New Orleans, La, USA, October 1997.

[11] Y. Liang and C. O. Nwankpa, "A new type of STATCOM based on cascading voltage-source inverters with phase-shifted unipolar SPWM," *IEEE Transactions on Industry Applications*, vol. 35, no. 5, pp. 1118–1123, 1999.

[12] P. W. Hammond, "A new approach to enhance power quality for medium voltage AC drives," *IEEE Transactions on Industry Applications*, vol. 33, no. 1, pp. 202–208, 1997.

[13] J. Rodríguez, J. Lai, and F. Z. Peng, "Multilevel inverters: a survey of topologies, controls, and applications," *IEEE Transactions on Industrial Electronics*, vol. 49, no. 4, pp. 724–738, 2002.

[14] I. Colak, E. Kabalci, and R. Bayindir, "Review of multilevel voltage source inverter topologies and control schemes," *Energy Conversion and Management*, vol. 52, no. 2, pp. 1114–1128, 2011.

[15] S. Sirisukprasert, J. Lai, and T. Liu, "Optimum harmonic reduction with a wide range of modulation indexes for multilevel converters," in *Proceedings of the 35th IAS Annual Meeting and World Conference on Industrial Applications of Electrical Energy (IEEE-IAS '00)*, pp. 2094–2099, October 2000.

[16] L. Li, D. Czarkowski, Y. Liu, and P. Pillay, "Multilevel selective harmonic elimination PWM technique in series-connected voltage inverters," in *Proceedings of the IEEE Industry Applications Conference*, pp. 1454–1461, October 1998.

[17] A. K. Gupta and A. M. Khambadkone, "A space vector PWM scheme for multilevel inverters based on two-level space vector PWM," *IEEE Transactions on Industrial Electronics*, vol. 53, no. 5, pp. 1631–1639, 2006.

[18] L. M. Tolbert and T. G. Habetier, "Novel multilevel inverter carrier-based PWM method," *IEEE Transactions on Industry Applications*, vol. 35, no. 5, pp. 1098–1107, 1999.

[19] V. G. Agelidis and M. Calais, "Application specific harmonic performance evaluation of multicarrier PWM techniques," in *Proceedings of Power Electronics Specialist Conference*, pp. 172–178, Fukuoka, Japan, May 1998.

[20] S. Tyrberg, R. Waters, and M. Leijon, "Wave power absorption as a function of water level and wave height: theory and experiment," *IEEE Journal of Oceanic Engineering*, vol. 35, no. 3, pp. 558–564, 2010.

[21] M. Rahm, C. Boström, O. Svensson, M. Grabbe, F. Bülow, and M. Leijon, "Laboratory experimental verification of a marine substation," in *Proceedings of the 8th European Wave and Tidal Energy Conference (EWTEC '09)*, pp. 51–58, Uppsala, Sweden, 2009.

[22] M. Rahm, O. Svensson, C. Boström, R. Waters, and M. Leijon, "Experimental results from the operation of aggregated wave energy converters," *IET Renewable Power Generation*, vol. 6, no. 3, pp. 149–160, 2012.

[23] R. Park, "Two reaction theory of synchronous machines," *AIEE Transactions*, vol. 48, no. 4, pp. 716–730, 1929.

[24] Z. Du, L. M. Tolbert, B. Ozpineci, and J. N. Chiasson, "Fundamental frequency switching strategies of a seven-level hybrid cascaded H-bridge multilevel inverter," *IEEE Transactions on Power Electronics*, vol. 24, no. 1, pp. 25–33, 2009.

[25] L. M. Tolbert, F. Z. Peng, T. Cunnyngham, and J. N. Chiasson, "Charge balance control schemes for cascade multilevel converter in hybrid electric vehicles," *IEEE Transactions on Industrial Electronics*, vol. 49, no. 5, pp. 1058–1064, 2002.